Bulk Lifetime and Doping in Crystalline Silicon via Two-Photon Absorption Time-Resolved Photoluminescence Decay

Robert Lee Chin, Michael Pollard, Michael P. Nielsen, and Ziv Hameiri

***Abstract*—Bulk lifetime (τ_{bulk}) and bulk doping (N_{dop}) are critical material parameters influencing solar cell performance. The ability to probe spatial variations in τ_{bulk} and N_{dop} in ingots, prior to wafer cutting and further processing, would be beneficial to improving the yield and reducing the cost of silicon solar cells. This study demonstrates the capability of the two-photon time-resolved photoluminescence decay method to determine both τ_{bulk} and N_{dop} in thick crystalline silicon samples. The use of two photon excitation enables a more uniform carrier generation profile compared to conventional single-photon excitation, making measurements less sensitive to surface effects. The method is verified using an unpassivated n-type Czochralski silicon disk and found to be in good agreement with the results obtained from the photoluminescence ratio imaging method.**

***Index Terms*—Bulk lifetime, crystalline silicon, two-photon absorption, time-resolvedphotoluminescence.**

I. Introduction

COMBINING two-photon absorption (TPA) and time-resolved photoluminescence (TRPL) in the so-called two-photon absorption time-resolved photoluminesence decay (TPA-TRPL) method, used as a tool for probing the bulk carrier dynamics in semiconductor materials far from the surface [1], [2]. In TPA-TRPL, an ultrafast laser in the pico- to femto-second pulse width regime operating at sub-bandgap wavelengths is focused inside the sample [3]. If the local optical intensity is sufficiently high, significant absorption may occur due to TPA, wherein the energy of two low-energy photons excites a single electron-hole pair across the bandgap [4]. With appropriate focusing of the beam, the location of the excess carrier generation can be concentrated well-below the surface of the sample. The resulting measured TRPL decay following the cessation of the excitation pulse is therefore more representative of the excess carrier concentration (Δn) dynamics occurring in the bulk, rather than being dominated by surface effects.

Manuscript received October 18, 2021; revised November 10, 2021; accepted December 2, 2021. Date of publication March 10, 2022; date of current version April 21, 2022. This work was supported by the Australian Government through Australian Renewable Energy Agency under Project 2017/RND001 and Project 2017/RND017. *(Corresponding author: Robert Lee Chin.)*

The authors are with the School of Photovoltaics and Renewable Energy Engineering, University of New South Wales, Sydney 2052, Australia (e-mail: rbtlch1n@gmail.com; m.e.pollard@unsw.edu.au; michael.nielsen@unsw.edu.au; z.hameiri@unsw.edu.au).

Color versions of one or more figures in this article are available at https://doi.org/10.1109/JPHOTOV.2021.3133545.

Digital Object Identifier 10.1109/JPHOTOV.2021.3133545

The typical materials studied by TPA-TRPL are direct-bandgap semiconductors including cadmium telluride (CdTe) [3], [5] and perovskite single crystals [2], [6]. To date, this method has not been applied to crystalline silicon, where it could be used to extract the bulk carrier lifetime (τ_{bulk}), a material parameter that is highly relevant for high-efficiency solar cells [7]. Our previous numerical study demonstrated that for crystalline silicon wafers with thicknesses of a few hundred microns, this method is unsuitable due to the long bulk diffusion length (L_d) relative to the wafer thickness (W), coupled with the large surface recombination velocities (SRV) of bare wafers [8]. Given that wafer thicknesses well below 200 μm are typical in photovoltaic applications, the method thus cannot provide reliable information about the material quality. However, for much thicker silicon samples, such as ingots or disks, this method has the potential for determining τ_{bulk} prior to slicing into wafers. It is noted that commercial systems [9] for measuring τ_{bulk} use the photoconductance decay (PCD) method [10] and often have poor spatial resolution due to their large sensor area (cm^2). The TPA-TRPL method can have a superior spatial resolution due to the spatially localized excitation.

Here, we use TPA to provide a relatively uniform generation profile across the thickness, rather than for bulk-localized excitation. This is because the investigated sample has a very large L_D/W ratio, meaning that bulk-focused excitation does not provide advantages over a uniform excitation (as discussed in more detail in Appendix A) [8]. Remarkably, τ_{bulk} can be extracted from the measured effective lifetime (τ_{eff}) without the need to consider the SRV under these circumstances [11]. The depth (z)-dependent generation rate is given by

$$G(z) = \frac{\beta_{\text{TPA}}}{2\hbar\omega}\left(\frac{H_{\text{peak}}}{1+\beta_{\text{TPA}}H_{\text{peak}}z}\right)^2 \tag{1}$$

where $\hbar\omega$ is the photon energy, H_{peak} is the peak intensity at the surface, corrected for the sample reflectance. β_{TPA} is the TPA coefficient with a unit of cm.W^{-1}. For silicon, β_{TPA} has a value of approximately 1 cm.GW^{-1} in the wavelength range 1200–1600 nm [12]. In contrast to the conventional excitation via single-photon absorption, the depth of the generation profile due to TPA can be tuned to a degree by varying H_{peak}. Additionally, the overall generation profile decreases with $1/z^2$, which is less rapid than the exponential decay (e^{-z}) of the single-photon absorption generation profiles.

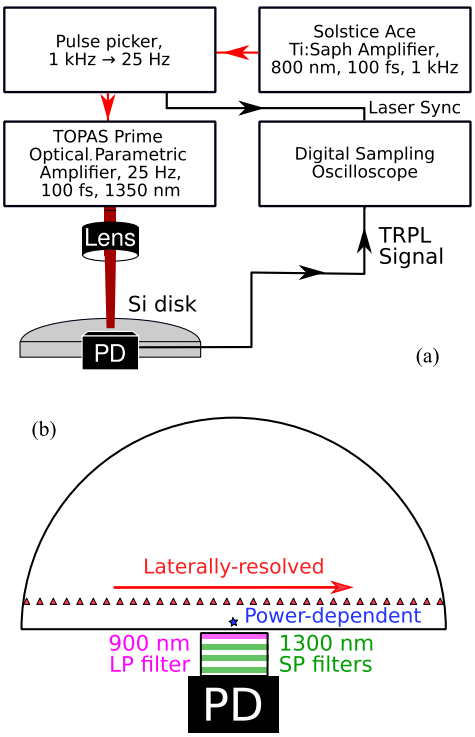

Fig. 1. (a) Schematic diagram of the experimental setup. (b) Locations for the power-dependent and laterally-resolved TPA-TRPL measurements, depicted by the blue star and red triangles, respectively. For the laterally resolved measurements, the detector-lens position was kept constant while the sample was mapped laterally. The edge-distance for the laterally resolved and power-dependent measurements were 12.5 and 1.5 mm, respectively.

In this article, the TPA-TRPL method is applied to a thick silicon sample to laterally resolve τ_{bulk} and the bulk doping (N_{dop}). Power-dependent measurements are first performed to demonstrate that the carrier generation occurs due to TPA. The results are then compared with a previous study that investigated the same sample using the PL image ratio (PLIR) method, which uses the ratio of the intensity of two PL images taken with different spectral filters, alongside a transfer function to laterally resolve τ_{bulk} [13].

The sample is a Czochralski (Cz) *n*-type silicon half-disk with 160 mm diameter and thickness of 20 mm (average $N_{\text{dop}} = 1.1 \times 10^{15}$ cm^{-3}). The bulk lifetime of this sample is up to 20 ms, as determined by PCD measurements. Further details on the sample (N674) are available in the study of Chung *et al.* [13].

II. Experiment

TPA-TRPL measurements were performed using the setup depicted in Fig. 1(a). A Solstice Ace titanium sapphire regenerative amplifier (peak wavelength of 800 nm, full-width at half-maximum pulse width of 100 fs, and a repetition rate of 1 kHz) is first reduced down to a repetition rate of 25 Hz using a pulse picker. This allows carrier lifetimes in the multimillisecond range to be resolved. The 800 nm pulse pumps a TOPAS Prime optical parametric amplifier to generate pulses with tuneable wavelength in the range 290–2600 nm. An excitation wavelength of 1350 nm was selected based on maximising β_{TPA}

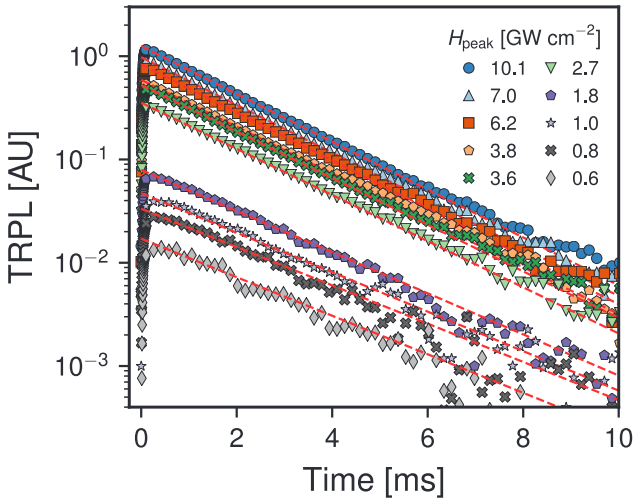

Fig. 2. H_{peak}-dependent TPA-TRPL decays. Mono-exponential decay fits are shown as dashed red lines.

(1.5 cm.GW^{-1}) while minimizing single photon absorption ($< 10^{-5}$ cm^{-1}). The excitation was weakly focused using a 100 mm focal length plano-convex lens, resulting in an full-width at half-maximum excitation spot diameter of 1730 ± 60 μm. The focal point was 15 mm behind the rear surface.

A thermoelectric-cooled silicon photodiode (PD) with integrated transimpedance amplifier (Hamamatsu S8785-25) was used for detection of the TPA-TRPL decays. This detector has a -3 dB bandwidth of 200 Hz and gain of 0.7 V.nW^{-1} at 1100 nm, allowing millisecond lifetimes to be directly resolved, while also having sufficiently high sensitivity to resolve the PL signal. A filter stack of three short-pass 1300 nm and a long-pass 900 nm filters (optical density of four for both types) were placed inside a lens tube and mounted in front of the detector to filter scattered excitation and ambient light, respectively. The detector setup was placed facing the cut-edge of the disk, perpendicular to the beam direction. The TRPL signal and the electronic synchronization signal from the laser were relayed to a digital sampling oscilloscope for data acquisition and triggering. For each TRPL decay, a measurement time of 100 s using 256 averages was applied.

Fig. 1(b) shows the regions of interest for the power-dependent (a blue star) and laterally resolved (red triangles) measurements. For the power-dependent measurements, H_{peak} was attenuated from 10 GW.cm^{-2} down to 0.6 GW.cm^{-2} using neutral density (ND) optical filters; these values include correction for the sample reflectance at 1350 nm. H_{peak} was approximately 10 GW.cm^{-2} for the laterally resolved TPA-TRPL measurements. The average laser power was observed to deviate by up to 20% from the mean value over the duration of the measurements, therefore, an uncertainty in the average laser power of $\pm 20\%$ was accounted for in the analysis.

III. Results and Discussion

We first analyze the power-dependent TPA-TRPL decays to verify that the carrier generation is due to TPA. Fig. 2 shows

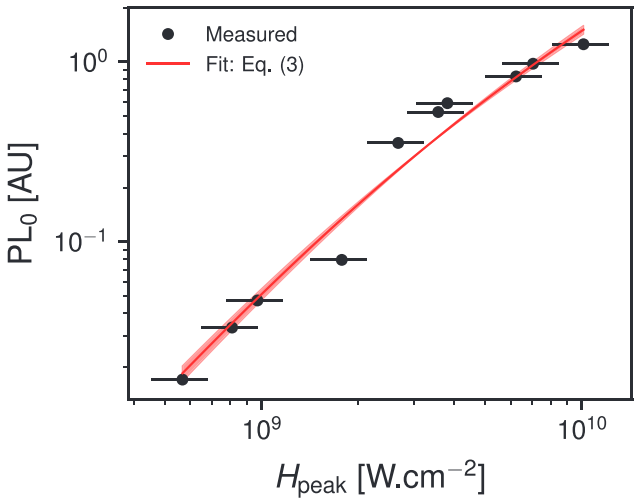

Fig. 3. H_{peak}-dependence of PL_0. The shaded red region represents the uncertainties in the fit.

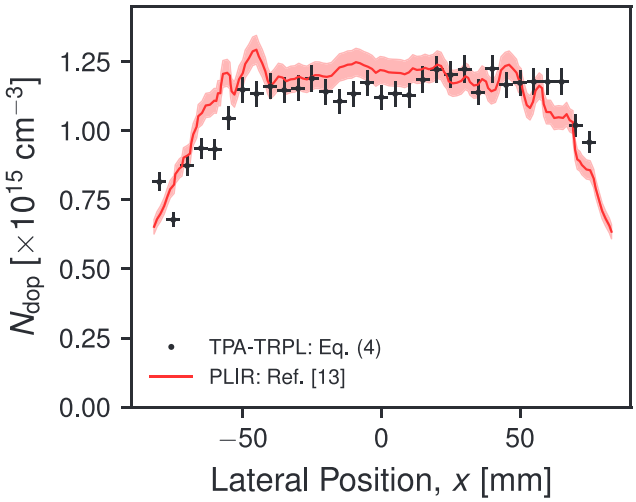

Fig. 4. Line-profiles of N_{dop}, as extracted from the TPA-TRPL and PLIR methods. Shaded red region represents the $\pm 4\%$ uncertainty of the PLIR measurement. The x-coordinate of zero represents the center of the disk.

the power-dependent TRPL decays (H_{peak}-dependent decays). Each TRPL decay was fit by a single exponential decay

$$\text{PL}(t) = \text{PL}_0 \exp\left(-\frac{t}{\tau_{\text{eff}}}\right) \tag{2}$$

where PL_0 is the amplitude of the TPA-TRPL decay. The unexpected increasing behavior of the TPA-TRPL at times < 0.1 ms is attributed to the attenuation of photon reabsorption as excess carriers diffuse away from the bulk toward the cut-edge (detector), coupled with negligible recombination [14]. The pure exponential decay at times > 0.1 ms is consistent with the low-injection condition ($\Delta n \ll N_{\text{dop}}$) within the disk [13]. The mean Δn following the carrier diffusion is estimated to be 8×10^{13} cm^{-3}, hence, the low-injection condition is satisfied. Further details regarding this estimation are included in Appendix B. Under these conditions, TPA-TRPL may be expressed as $\text{PL}_0 = A_i \cdot \Delta n_0 \cdot N_{\text{dop}}$, where A_i is a calibration constant containing the detection system optical efficiencies, the photon reabsorption factor [15], and the radiative recombination coefficient of silicon [16], while Δn_0 represents the average Δn when the recombination becomes dominant over the carrier diffusion.

Fig. 3 shows the H_{peak}-dependence of PL_0. Assuming the absorption process is only due to TPA and the carrier density is in the low-injection regime, PL_0 can be estimated from (1) as t_{pulse} is much shorter than τ_{eff}

$$\text{PL}_0(H_{\text{peak}}) = A \int_0^W \left(\frac{H_{\text{peak}}}{1 + \beta_{\text{TPA}} H_{\text{peak}} z}\right)^2 \mathrm{d}z \tag{3}$$

where A is a scaling constant. The derivation of (3) can be found in Appendix C. The measurements can be fit relatively well using this equation and the extracted $\beta_{\text{TPA}} = (0.18 \pm 0.05)$ cm.GW^{-1} is within the expected order of magnitude [12]. This demonstrates that the TPA process is responsible for the carrier generation. It is noted that third harmonic generation (THG) could also affect the shape of the PL signal at high H_{peak}. However, we demonstrate in Appendix D that THG is unlikely to be significant in our measurements.

Next, the laterally resolved TPA-TRPL measurements were analysed to extract N_{dop} and τ_{bulk}. Fig. 4 shows the laterally resolved line-profile of N_{dop} extracted from the proportionality of PL_0 with N_{dop}

$$N_{\text{dop}}(x) = \frac{\text{PL}_0(x)}{\overline{\text{PL}_0(x)}} \cdot \overline{N_{\text{dop}}} \tag{4}$$

where $\text{PL}_0(x)$ is the PL_0 profile, $\overline{\text{PL}_0(x)}$ is the average PL_0, and $\overline{N_{\text{dop}}}$ is the average doping, as measured by a complementary technique such as the dark photoconductance. This analysis assumes that Δn_0 and A_i are spatially uniform, which is justified as Δn_0 depends mostly on the incident optical power, the excitation pulse width, and the sample reflectance (assumed to be constant), while A_i depends only on the sample thickness and the detection optics.

This is compared with the line-profile from the PLIR method. Both measurements were scaled to a unit of cm^{-3} using $\overline{N_{\text{dop}}}$ from the dark photoconductance [13]. All measurement points lie within $\pm 15\%$ of the reference PLIR method, thus, demonstrating reasonable agreement between the two methods. It is worth noting that both TPA-TRPL and PLIR measure the average N_{dop} weighted by the excess carrier profile. Since both methods yield similar lateral doping profiles despite the different excess carrier profiles (TPA-TRPL's profile is more uniform over the depth, whereas the PLIR's profile is closer to the surface) it seems that N_{dop} is uniform across the sample depth.

The extraction of τ_{eff} requires first quantifying the surface lifetime (τ_{surface}), which for a sample with symmetric surfaces is given by [11]

$$\tau_{\text{surface}} = \frac{W}{2 \cdot \text{SRV}} + \frac{1}{D_a}\left(\frac{\pi}{W}\right)^2 \tag{5}$$

where D_a is the low-injection ambipolar carrier diffusivity, which is a function of N_{dop} [17], [18]. Note that this equation assumes only one dimension (the sample depth). Within a few L_d from the edges, τ_{surface} is lower than predicted by (5) due to additional surface recombination at the edges. Using (5) results

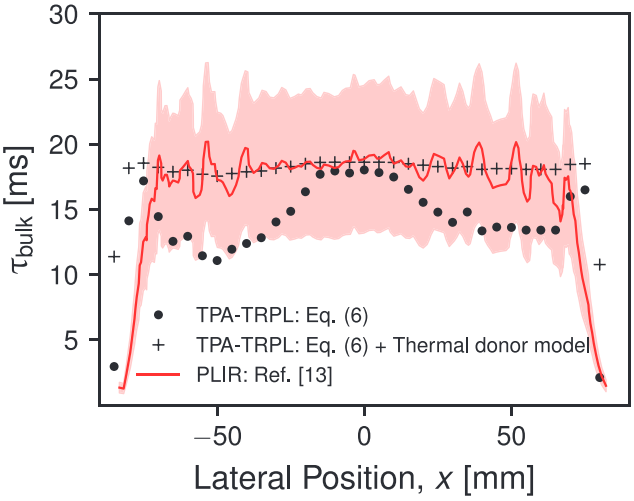

Fig. 5. Line-profiles of τ_{bulk} as extracted from the TPA-TRPL [(2) and (6)] and PLIR methods. The shaded red region represents the $\pm 30\%$ uncertainty of the PLIR measurement. The x-coordinate of zero represents the center of the disk. In both measurements, the sharp decrease of τ_{bulk} close to the edges are edge effects caused by the diffusion of carriers that are very close to the unpassivated wafer edges [13].

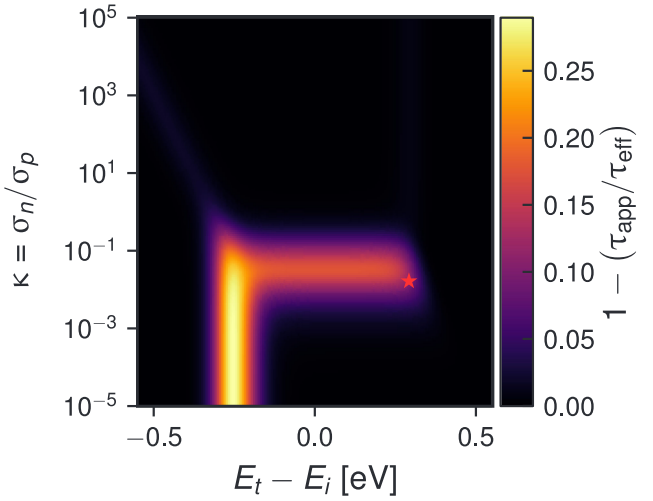

Fig. 6. Simulated colour-map of $[1 - (\tau_{\text{app}}/\tau_{\text{eff}})]$ as a function of κ and $E_t - E_i$. The red star indicates thermal donors at a concentration of 10^{14} cm^{-3} [22].

in the so-called "edge artefacts" [13], where the calculated τ_{bulk} decreases rapidly approaching the edges. Accounting for this additional recombination cannot be done analytically like it is assumed in (5). One way this can be done is using three dimensional numerical analysis (finite different or finite element) of the continuity equation, similar to the modeling demonstrated in [19]. Such analysis is beyond the scope of this article.

The first term in (5) represents the contributions due to the SRV, while the second term indicates the rate of diffusion of excess carriers to the surfaces. The SRV of the disk is estimated to be $> 10^3$ cm.s^{-1} considering a thin native oxide layer on the surface [20]. The second term represents the diffusion of carriers and is $\sim$145 ms for D_a equal to 17 cm^2.s ($N_{\text{d}} = 1.1 \times 10^{15}$ cm^{-3}). Thus, the SRV term is less than 0.6% of the diffusion term, meaning that $\tau_{\text{surface}} \approx \frac{1}{D_a}(\frac{\pi}{W})^2$. Hence, τ_{bulk} may be calculated from the measured τ_{eff} [extracted using (2)] using [11]

$$\tau_{\text{bulk}} = \left[\tau_{\text{eff}}^{-1} - D_a\left(\frac{W}{\pi}\right)^2\right]^{-1}. \tag{6}$$

Fig. 5 shows the line-profile of τ_{bulk} (black circles) compared to the reference PLIR method (red line). The two methods produce a similar magnitude of τ_{bulk} considering the $\pm 30\%$ uncertainty in the PLIR method. However, significant deviations are observed between the shape of the line-profiles from the two methods.

The most likely reason for this discrepancy is due to transient charge carrier trapping, which can affect the TRPL decay in low-injection [21]. In order to justify this hypothesis, we simulated low-injection TRPL decays with and without charge trapping covering a wide range of capture cross-sectional ratios [$\kappa = \sigma_n/\sigma_p$, where σ_n (σ_p) is the electron (hole) capture cross section] and defect energy levels ($E_t - E_i$, where E_t is the trap energy and E_i is the intrinsic energy level). To simulate bulk charge carrier trapping, we assumed a single Shockley–Read–Hall (SRH) defect with the following recombination parameters.

1) The defect is an donor (hole trap).
2) Total defect density of $N_t = 10^{14}$ cm^{-3}.
3) Hole capture cross section, $\sigma_p = 3 \times 10^{-20}$ cm^2. This value is based on the above N_t and assuming the low-injection bulk lifetime, τ_{p0}, is equal to 20 ms [13].
4) Variable energy level $E_t - E_i$ from -0.55 eV (valence band-edge) to 0.55 eV (conduction band-edge).
5) Variable capture cross-section ratio, κ, from 10^{-5} to 10^5.

We then extracted the TRPL decay constants, where τ_{app} and τ_{eff} are defined as the decay constants with and without charge trapping, respectively. The term $[1 - (\tau_{\text{app}}/\tau_{\text{eff}})]$ quantifies the degree of charge trapping, with large positive values indicating a strong charge trapping effect. Detailed information about the simulation can be found in Appendix E.

Fig. 6 shows the results of the simulations. Note that the yellow rectangle on the left-hand side is irrelevant to this discussion as it corresponds to a bi-exponential decay behavior, which has not been observed in any of our TPA-TRPL measurements. The orange rectangle region on the right is the relevant region and corresponds to a defect with a very small κ and energy level in the upper bandgap half. In the PLIR study, it was postulated that thermal donors are the bulk defect contributing to both the bulk recombination and nonuniform lateral doping. We have plotted the coordinate (red star) for thermal donors with N_t of 10^{14} cm^{-3}, which is inside the top right of this region [22]. This value of N_t is estimated based on the value of Δn corresponding to the uptick of the PCD injection-dependent lifetime presented in the study of Chung *et al.* [13]. This may suggest that the discrepancy in τ_{bulk} is due to charge carrier trapping from bulk defects, such as thermal donors, which influence τ_{eff} in the TPA-TRPL measurements. We highlight that this relatively strong charge trapping effect is in part due to the combined effects of the high trap density relative to the bulk doping ($\sim$10%) and a very small κ.

It is possible to eliminate the charge trapping effect by using the published values of the defect parameters for thermal donors [22]. By varying the thermal donor density, a transfer function for converting τ_{bulk} from TPA-TRPL to the steady-state τ_{bulk} can be determined. More details on how this transfer function was calculated is in Appendix E. The "+" markers in Fig. 5 shows τ_{bulk} from TPA-TRPL corrected for thermal donors. The thermal donor corrected τ_{bulk} shows a very good correspondence with the PLIR τ_{bulk}. This strongly suggests that the difference between the TPA-TRPL and PLIR τ_{bulk} is due to thermal donors.

For defects without strong charge trapping behavior, the TPA-TRPL method may be expected to yield a more accurate τ_{bulk} compared to the PLIR method. This is because in the TPA-TRPL method, τ_{eff} is extracted from the slope of the TPA-TRPL decays in low-injection. Therefore, it is unaffected by any of the calibration constants A_i, Δn_0 or N_{dop}. In the TPA-TRPL measurements, this lead to a typical uncertainty of less than 2%. In contrast, the PLIR method calculates τ_{bulk} using a transfer function correlated to the ratio of two steady-state PL intensity images taken with different spectral filters [23]. The main uncertainties are associated with the spectral sensitivities of the cameras and filters, leading to a significantly larger uncertainty compared to the TPA-TRPL method of up to $\pm 30\%$.

IV. Conclusion

In summary, this article demonstrated the application of the TPA-TRPL method to crystalline silicon. Power-dependent measurements confirmed that the carrier generation is due to TPA. Subsequently, laterally dependent TPA-TRPL measurements were used to extract line-profiles of τ_{bulk} and N_{dop} across a silicon disk. These results were compared with reference measurements using the PLIR method. Relatively good agreement was found for N_{dop}, whereas τ_{bulk} showed a discrepancy in the shape of the line-profile, relative to the PLIR method. This discrepancy is most likely due to transient charge trapping effects induced by bulk defects, such as thermal donors. After correcting τ_{bulk} from TPA-TRPL for trapping from thermal donors, we obtained a τ_{bulk}, which agreed very well with the PLIR measurements, thus, demonstrating that thermal donors were responsible for the discrepancy.

We emphasise that for samples without strong charge trapping, the TPA-TRPL method has lower uncertainty in τ_{bulk} due to the extraction of τ_{eff} from the slope of the TRPL decay.

For future studies, 2-D mapping could be performed to extract additional laterally resolved information about the sample. The 3-D mapping combined with depth-localized excitation is a viable option for bricks or ingots with smaller L_d/W ratio to minimize carrier diffusion to the cut surfaces. This would require the position of the lens relative to the PD to be fixed to keep photon reabsorption effects constant and customized optics to focus several cm into the sample bulk. Another possibility is to extend the method to analyse injection-dependent lifetimes, which requires careful determination of the Δn_0 profile for calibration. Finally, given that the TPA-TRPL decays may be affected by charge carrier trapping, it could be used for investigating the recombination parameters of defects with charge trapping behavior.

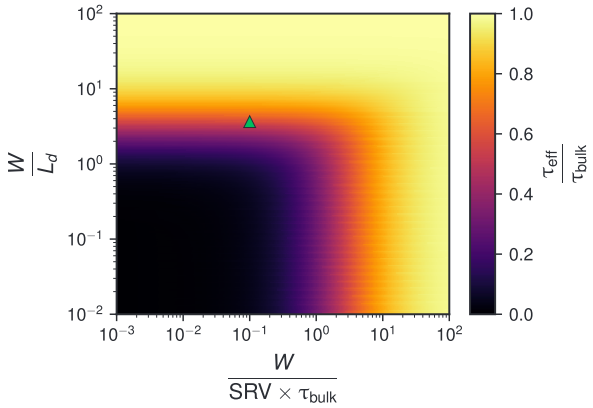

Fig. 7. Color-map of the ratio of τ_{eff} to τ_{bulk} for varying W/L_d and $W/(\text{SRV} \times \tau_{\text{bulk}})$ ratios. The green triangle indicates the coordinate for the measured sample.

Appendix A
Lifetime Ratio for Varying τ_{bulk} and SRV

In this section, we show that $\tau_{\text{eff}} = \tau_{\text{bulk}}$ cannot be assumed for the measured sample. In our previous study, we showed that even under bulk-localized excitation, the ratio of τ_{eff} to τ_{bulk} is given by [8]

$$\frac{\tau_{\text{eff}}}{\tau_{\text{bulk}}} = \frac{1}{1 + \left[\frac{1}{2}\frac{W}{\text{SRV} \times \tau_{\text{bulk}}} + \frac{1}{\pi^2}\left(\frac{W}{L_d}\right)^2\right]^{-1}}. \tag{7}$$

Fig. 7 shows that for the sample measured in this article, $\frac{\tau_{\text{eff}}}{\tau_{\text{bulk}}} \approx 0.6$, meaning that the measured τ_{eff} is always smaller than τ_{bulk}, even with bulk-localized excitation. This justifies the use of bulk-uniform excitation rather than bulk localized excitation, which would be more difficult to implement in the experiment.

Appendix B
Estimation of the Mean Excess Carrier Density

Throughout this article, we assumed that the sample is in the low-injection regime. In this section, we show the calculations used to verify this assumption.

The large L_d relative to W of the investigated sample means that carriers redistributes via carrier diffusion following the excitation pulse without significant recombination. At long times ($> 100\ \mu$s), there is mostly recombination without significant carrier redistribution. The maximum carrier density following this redistribution is the relevant carrier density for determining if the excess carriers are in the low- or high-injection regime.

First, the total number of excess carrier generated by the excitation pulse (ΔN_0) needs to be calculated. This is given by integrating the initial excess carrier density over the excitation volume

$$\Delta N_0 = \frac{\pi}{4} D_{\text{spot}}^2 \int_0^W G(z) \cdot t_{\text{pulse}}\, \mathrm{d}z. \tag{8}$$

D_{spot} is the excitation spot size, and $G(z)$ is the TPA generation profile. An explicit expression for $G(z)$ is given by (1). For the maximum H_{peak} in this study of 10 GW.cm^{-2}, we calculate $\Delta N_0 = 7.8 \times 10^{13}$.

The carrier profile following carrier diffusion is more difficult to estimate because carrier diffusion occurs in all three dimensions. Along the z-axis, we estimate a uniform carrier profile. Laterally (coordinate r), we estimate an sech function, which is similar to an exponential decay but flattens near $r = 0$

$$\Delta n_{\text{after diff}}(r) = \Delta n_{0,\text{diff}} \cdot \operatorname{sech}\left(\frac{r}{L_d}\right). \tag{9}$$

$\Delta n_{0,\text{diff}}$ is the peak Δn following the carrier redistribution. This is calculated as

$$\Delta n_{0,\text{diff}} = \frac{\Delta N_0}{\displaystyle\int_0^\infty \operatorname{sech}\left(\frac{r}{L_d}\right) r \, \mathrm{d}r}. \tag{10}$$

From (10), we calculated $\Delta n_{0,\text{diff}} = 2.1 \times 10^{14}$ cm^{-3}.

Finally, the mean excess carrier density ($\overline{\Delta n_{0,\text{diff}}}$) relevant for PL is [19]

$$\overline{\Delta n_{0,\text{diff}}} = \frac{\displaystyle\int_0^\infty \Delta n_{\text{after diff}}(r)^2 \left[\Delta n_{\text{after diff}}(r) + N_{\text{d}}\right] r \, \mathrm{d}r}{\displaystyle\int_0^\infty \Delta n_{\text{after diff}}(r) \left[\Delta n_{\text{after diff}}(r) + N_{\text{d}}\right] r \, \mathrm{d}r}. \tag{11}$$

Using (11), we calculated $\overline{\Delta n_{0,\text{diff}}} = 8.4 \times 10^{13}$ cm^{-3}. Typically, the factor $\frac{\Delta n}{N_{\text{d}}} < 0.1$ is accepted as low-injection. We calculated $\frac{\overline{\Delta n_{0,\text{diff}}}}{N_{\text{d}}} = \frac{8.4\times10^{13}}{1.1\times10^{15}} = 0.08$, hence, validating the low-injection condition.

Appendix C
Derivation of the Equations for PL_0 and the Time-Integrated PL

In this section, we derive (3) for PL_0 as a function of H_{peak}. We also derive the expression for the time-integrated PL versus the laser pulse fluence, ϕ_{ex}. Both equations are derived under the assumption of low-injection conditions (PL $\propto \Delta n$).

To present PL_0 as a function of H_{peak}, it is assumed that the excitation beam is collimated. Thus, the intensity at the surface, $H(0)$, is equal to H_{peak}. The equation of the absorption rate in TPA is [4]

$$\frac{\partial H}{\partial z} = -\beta_{\text{TPA}} H^2. \tag{12}$$

The expression for the generation rate under TPA condition is identical to the case of single-photon excitation, except for the division by twice the photon energy, $\hbar\omega$

$$G = -\frac{\beta_{\text{TPA}}}{2\hbar\omega}\frac{\partial H}{\partial z}. \tag{13}$$

The excess carrier density generated by the pulse, Δn_0, is unaffected by the carrier kinetics since the pulse width, t_{pulse}, is much shorter than τ_{eff} (the full-width half maximum pulse width is 100 fs, which corresponds to a decay constant of 42 fs)

$$\Delta n_0 = G \cdot t_{\text{pulse}}. \tag{14}$$

Note that there are possible spatial variations in τ_{bulk} (sample) and the Gaussian beam shape (illumination). Spatial variations in τ_{bulk} are not expected to alter Δn_0 because the photo-generation occurs more than a billion times faster than the bulk recombination. The Gaussian beam shape of the illumination profile can be accounted for by changing the equation for Δn_0 to a function of the lateral position, (x, y): $\Delta n_0 = \Delta n_0(x, y) = G_0 \exp\left(-\frac{x^2}{2\sigma_x^2} - \frac{y^2}{2\sigma_y^2}\right) \cdot t_{\text{pulse}}$, where G_0 is the peak generation rate, and σ_x and σ_y are the standard deviations in the x- and y-directions, respectively. However, in this article, we opt to use the average values for the generation rate and spot size, rather than a spatially dependent generation rate as this simplifies the analysis from three dimensions to one dimension.

Solving (12) alongside the initial condition $H(0) = H_{\text{peak}}$ leads to the following expressions for the the intensity:

$$H(H_{\text{peak}}, z) = \frac{H_{\text{peak}}}{1 + H_{\text{peak}}\beta_{\text{TPA}} z}. \tag{15}$$

Equations (13) and (15) leads to (1) for the generation rate

$$G(H_{\text{peak}}, z) = \frac{\beta_{\text{TPA}}}{2\hbar\omega}\left(\frac{H_{\text{peak}}}{1 + H_{\text{peak}}\beta_{\text{TPA}} z}\right)^2. \tag{1}$$

Equations (1) and (14) leads to the following equation for PL_0 as a function of H_{peak} and z:

$$\begin{aligned}\text{PL}_0(H_{\text{peak}}, z) &= \frac{A_i \beta_{\text{TPA}} N_{\text{dop}} t_{\text{pulse}}}{2\hbar\omega}\left(\frac{H_{\text{peak}}}{1 + \beta_{\text{TPA}} H_{\text{peak}} z}\right)^2 \\ &= A\left(\frac{H_{\text{peak}}}{1 + \beta_{\text{TPA}} H_{\text{peak}} z}\right)^2.\end{aligned} \tag{16}$$

To remove the depth-dependence of PL_0, the expression for PL_0 is numerically integrated over the sample thickness (W), leading to (3)

$$\text{PL}_0(H_{\text{peak}}) = A\int_0^W \left(\frac{H_{\text{peak}}}{1 + \beta_{\text{TPA}} H_{\text{peak}} z}\right)^2 \mathrm{d}z. \tag{3}$$

We now derive the expression for PL_0 used in the standard bulk-localized TPA-TRPL method [3], which assumes $\text{PL}_0 = \gamma\phi_{\text{ex}}^2$, where γ is a positive constant. This square law arises from the assumptions of the following.

1) The excitation profile, $H(z)$, does not change its shape with increasing ϕ_{ex}, meaning that the intensity can be expressed as $H(z) = m\phi_{\text{ex}}$, where m is a positive constant.
2) τ_{eff} is injection-independent.

Combining the above assumptions alongside (12)–(14) leads to the following expressions for the TRPL decay and the time-integrated PL:

$$\begin{aligned}\text{PL}(t) &= A_i N_{\text{dop}} \Delta n(t) \\ &= A_i N_{\text{dop}} G \tau_{\text{pulse}} \exp\left(-\frac{t}{\tau_{\text{eff}}}\right)\end{aligned} \tag{17}$$

$$\begin{aligned}\text{Time-Integrated PL} &= \frac{A_i N_{\text{dop}} G t_{\text{pulse}}}{\tau_{\text{eff}}} \\ &= \frac{A_i \beta_{\text{TPA}} N_{\text{dop}} m^2 t_{\text{pulse}}}{2\hbar\omega\tau_{\text{eff}}}\phi_{\text{ex}}^2 \\ &= \gamma\phi_{\text{ex}}^2.\end{aligned} \tag{18}$$

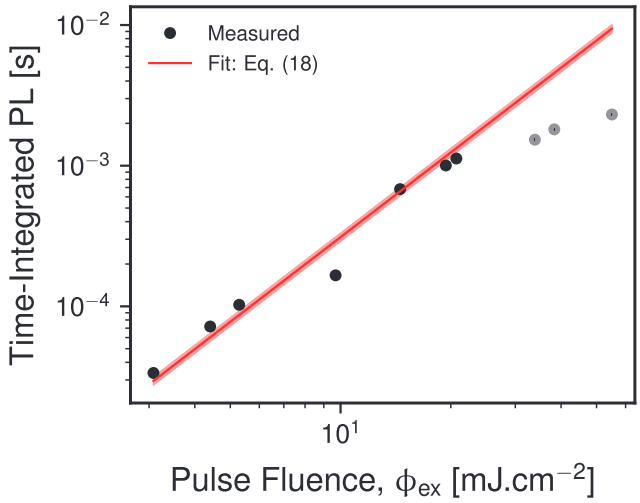

Fig. 8. H_{peak}-dependence of the time-integrated PL compared to the square-law scaling of the bulk-localised TPA-TRPL method. Gray markers represent measurements not considered by the square-law curve-fit.

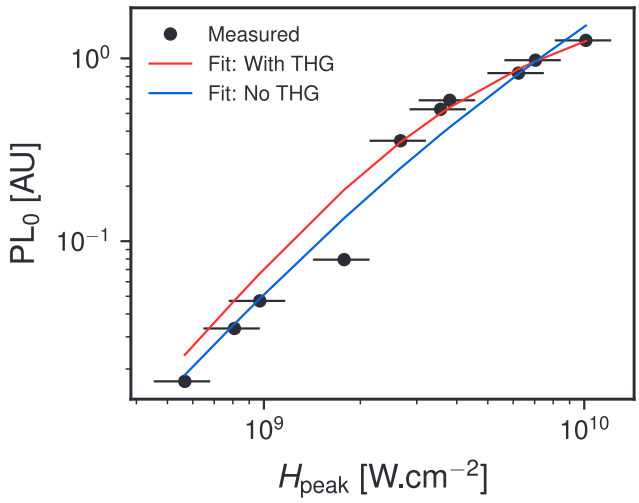

Fig. 9. PL_0 versus H_{peak}, curve-fitted with and without the THG process.

Fig. 8 shows the ϕ_{ex}-dependence of the time-integrated PL as compared with the square-law relation predicted by the bulk-excitation TPA-TRPL method. Note that only the seven lowest data points are used for this curve-fit. The deviation from the square law at high ϕ_{ex} (> 10 mJ.cm^{-2}) is attributed to the change in the shape of the generation profile at high ϕ_{ex}.

Appendix D
Effect of the THG Process on the PL_0 Versus H_{peak} Signal

THG is a nonlinear optical process that occurs alongside TPA. In THG, three low energy photons are absorbed and converted into a single photon with energy equal to the sum of the three low energy photons [4]. Therefore, the absorption is assumed to scale with the cube of H_{peak}. The rate equation to calculate the intensity considering both TPA and THG processes is

$$\frac{\partial H}{\partial z} = -\beta_{TPA} H^2 - \gamma_{THG} H^3. \tag{19}$$

γ_{THG} represents the strength of the THG process. The PL_0 signal can then be extracted by plugging the above solution into (13) and (14), assuming the sample is in the low-injection regime.

Fig. 9 shows the PL_0 versus H_{peak} curve-fitted with (19). In one instance, we deactivated the THG process. Comparing both cases, it is observed that including THG yields the better fit to the measurements. However, the extracted β_{TPA} is (0.0013 ± 0.1) cm.GW^{-1}, which is three orders of magnitude smaller than expected [12] and has an unacceptable standard error. In contrast, the curve-fit without THG produced a β_{TPA} of (0.18 ± 0.05) cm.GW^{-1}, which is within an order of magnitude of the expected value from [12]. This suggests that the inclusion of the THG process yields an improved fit due to overfitting the measurement. Therefore, we argue that THG is not relevant for this study, meaning that (3) is sufficient for explaining the H_{peak}-dependence of PL_0.

Appendix E
Simulations of Charge Carrier Trapping

In this article, we assumed that the TPA-TRPL decay constant is due to the minority carrier recombination. However, transient PL methods, such as TPA-TRPL may be also be affected by charge carrier trapping in low-injection [21]. We performed numerical simulations of the TRPL decays with and without charge trapping effects using similar parameters to the actual measurement, i.e., N_{dop} (1.1×10^{15} cm^{-3}), $\tau_{surface}$ (27.5 ms), laser repetition rate (25 Hz), and sample temperature of 300 K. An injected excess carrier concentration ($\Delta n_0 = 8 \times 10^{13}$ cm^{-3}) due to each laser pulse was applied, as previously estimated. Note that the effect of traps during the optical generation may be neglected due to the very short time duration of the pulse (100 fs) relative to the recombination (> 100 μs).

We also simulate Δn profiles after many cycles to account for Δn accumulated from the end of multiple laser cycles. The number of cycles was adjusted such that the difference between the trapped hole density (p_t) accumulated at the end of the current (N) and previous ($N-1$) cycle was less than 0.1% of the difference of p_t between the first two cycles. This ensured that the background Δn at the end of the TRPL decay has reached close to a steady-state. As all Δn are in the low-injection regime, the Δn decays are used as a proxy for the TPA-TRPL decays (TRPL $\propto \Delta n$).

We solved the Shockley–Read–Hall rate equation for trapped holes and zero-dimensional continuity equation for excess carriers under transient excitation ($G = 0$, known Δn_0)

$$\frac{\partial p_t}{\partial t} = \sigma_p v_{th,p}(N_t - p_t)p - \sigma_p v_{th,p} p_1 p_t - \sigma_n v_{th,n} p_t n + \sigma_n v_{th,n} n_1 (N_t - p_t) \tag{20}$$

$$\frac{\partial \Delta n}{\partial t} = -\sigma_p v_{th,p}(N_t - p_t)p + \sigma_p v_{th,p} p_1 p_t - \frac{\Delta n}{\tau_{surface}}. \tag{21}$$

Without charge trapping, we solve the 0-D continuity equation for excess carriers combined with the Shockley–Read–Hall

recombination equation

$$\frac{\partial \Delta n}{\partial t} = -\frac{\Delta n\,(\Delta n + N_{\text{dop}})}{\tau_{p0}\,(n + n_1) + \tau_{n0}\,(p + p_1)} - \frac{\Delta n}{\tau_{\text{surface}}}. \tag{22}$$

$\tau_{p0} = \frac{1}{\sigma_p v_{\text{th,p}} N_t}$ and $\tau_{n0} = \frac{1}{\sigma_n v_{\text{th,n}} N_t}$. n_1 (p_1) is the SRH statistical factor for electrons (holes) [24].

Fig. 10 shows the results of the simulation as separate Δn-decay plots. Note that in the main text, we have presented these results as a color-map. The solid (dashed) lines in Fig. 10 show Δn with (without) charge carrier trapping. In most cases, we observe that the solid and dashed lines are overlapped and can be described by a mono-exponential decay, meaning that charge carrier trapping does not affect the TPA-TRPL measurements. For some defect energies closer to the valence band edge ($\kappa < 10, E_t - E_i < -0.25$ eV) the solid curves are offset above the dashed curves but have the same decay constant. This offset is due to the background Δn accumulated after many laser cycles. In some instances ($\kappa < 10^{-3}$, $E_t - E_i = -0.25$ eV), the solid curves show a bi-exponential behavior. This is indicative of the trapping effect, where the first decay constant is related to recombination while the second decay constant is due to recombination of de-trapped carriers [21]. For some of the dashed curves ($\kappa = 10^{-5}$, $E_t - E_i$ from -0.05 to 0.35 eV), the dashed curves are slightly nonlinear on the logarithmic y-axis, whereas the solid curves are mono-exponential. This slight nonlinearity can be attributed to the injection-dependence of the SRH lifetime (τ_{SRH}) in low-injection for small κ: $\tau_{\text{SRH}} = \tau_{\text{p0}}(\frac{1}{\kappa}\frac{\Delta n}{N_{\text{dop}}} + 1) \approx \frac{\Delta n}{10^{12}}\tau_{p0}$ for $\kappa = 10^{-3}$ and $N_{\text{dop}} = 10^{15}$ cm^{-3}. We note that all of our measured TPA-TRPL decays have a mono-exponential decay behavior. Hence, only the latter discrepancy can be considered consistent with charge trapping for our TPA-TRPL measurements. This corresponds to the purple rectangle region of the color-map in the main text.

Appendix F
Transfer Function to Correct τ_{BULK} From TPA-PLIR for Thermal Donors

The effect of thermal donors on the TPA-TRPL may be corrected by determining the transfer function that converts the τ_{bulk} from the TPA-TRPL decays to the steady-state τ_{bulk}. The TPA-TRPL decays were simulated as described in Section E for N_t varied from 10^{12} to 10^{14} cm^{-3}. τ_{bulk} was extracted from the TPA-TRPL decays corrected for τ_{surface}. At each N_t, the steady-state lifetime, $\tau_{\text{bulk,SS}}$, was also calculated using the Shockley–Read–Hall equation [24], with published values for the thermal donor defect parameters [22]. The used values are as follows:

$$X = 0.1268 \cdot N_t + 3.956 \times 10^{13}$$

$$\sigma_n = 3.16 \times 10^{-54} \cdot X^{2.41}$$

$$\sigma_p = 4.01 \times 10^{-40} \cdot X^{1.53}$$

$$E_t = \frac{1.12}{2} - 16.46 \cdot N_t^{-0.12}.$$

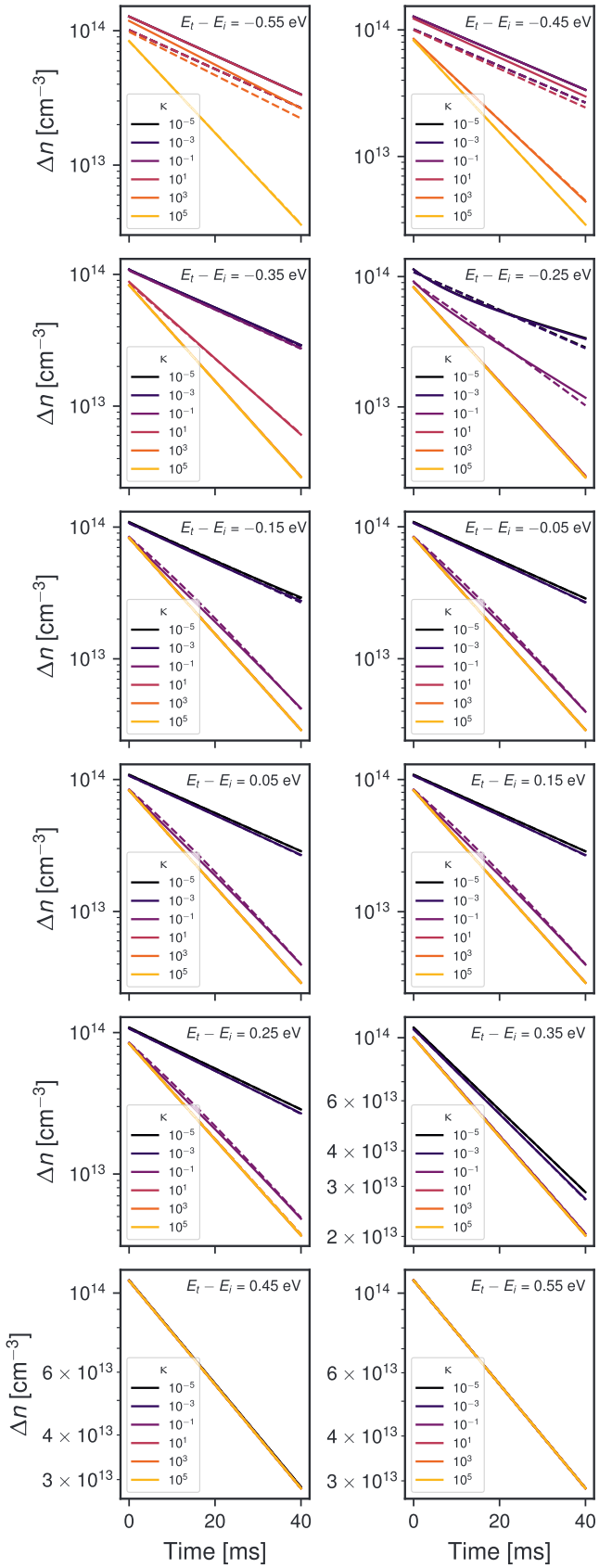

Fig. 10. Δn decays at varying κ and $E_t - E_i$. Solid and dashed lines represent the Δn decays with and without trapping, respectively. Note the bi-exponential decay of the solid lines for $E_t - E_i = -0.25$ eV and $\kappa < 10^{-3}$, indicative of charge trapping.

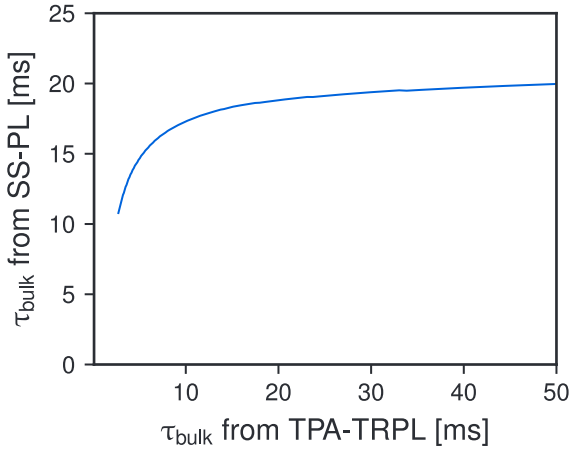

Fig. 11. Simulated transfer function used to convert the τ_{bulk} from TPA-TRPL to τ_{bulk} from the steady-state PL.

While the equation below is used to calculate $\tau_{\text{bulk,SS}}$

$$\tau_{\text{bulk,SS}} = \frac{\tau_{p0}\left(\Delta n + N_{\text{dop}} + n_1\right) + \tau_{n0}\left(\Delta n + p_1\right)}{\Delta n + N_{\text{dop}}} \tag{23}$$

where X is one of the structural configurations of the thermal donor defect (the other configuration is H) [22].

In order to match the PLIR measurements, a constant generation rate (constant light intensity) was required for $\tau_{\text{bulk, SS}}$. A light-intensity of 10 mW.cm^{-2} at 900 nm was used in order to match the minimum Δn for the PLIR method in [13, Fig. 5]. $\tau_{\text{bulk,SS}}$ was determined by numerical iteration of the steady-state continuity equation: $\tau_{\text{bulk, SS}} = \frac{\Delta n}{G}$, where G is the constant generation rate. This produced the transfer function shown in Fig. 11.

ACKNOWLEDGMENT

The authors would like to thank Thorsten Trupke (UNSW) for constructive feedback. M.P.N. thanks the UNSW Scientia Program for on-going support. The views expressed herein are not necessarily the views of the Australian Government, and the Australian Government does not accept responsibility for any information or advice contained herein.

REFERENCES

[1] D. Kuciauskas, A. Kanevce, P. Dippo, S. Seyedmohammadi, and R. Malik, "Minority-carrier lifetime and surface recombination velocity in single-crystal cdTe," *IEEE J. Photovolt.*, vol. 5, no. 1, pp. 366–371, Jan. 2015.

[2] Y. Yamada *et al.*, "Dynamic optical properties of CH $_3$ NH_3PbI_3 single crystals as revealed by one- and two-photon excited photoluminescence measurements," *J. Amer. Chem. Soc.*, vol. 137, no. 33, pp. 10456–10459, 2015.

[3] E. S. Barnard *et al.*, "Probing carrier lifetimes in photovoltaic materials using subsurface two-photon microscopy," *Sci. Rep.*, vol. 3, no. 1, pp. 1–9, 2013.

[4] R. W. Boyd, *Nonlinear Optics*, 3rd ed. New York, NY, USA: Academic Press, 2008.

[5] D. Kuciauskas *et al.*, "Minority carrier lifetime analysis in the bulk of thin-film absorbers using subbandgap (two-photon) excitation," *IEEE J. Photovolt.*, vol. 3, no. 4, pp. 1319–1324, Oct. 2013.

[6] T. Yamada *et al.*, "Fast free-carrier diffusion in $CH_3NH_3Br_3$ single crystals revealed by time-resolved one- and two-photon excitation photoluminescence spectroscopy," *Adv. Electron. Mater.*, vol. 2, no. 3, 2016, Art. no. 1500290.

[7] A. Blakers, N. Zin, K. R. McIntosh, and K. Fong, "High efficiency silicon solar cells," *Energy Procedia*, vol. 33, pp. 1–10, 2013.

[8] R. L. Chin, M. Pollard, T. Trupke, and Z. Hameiri, "Numerical simulations of two-photon absorption time-resolved photoluminescence to extract the bulk lifetime of semiconductors under varying surface recombination velocities," *J. Appl. Phys.*, vol. 125, no. 10, 2019, Art. no. 105703.

[9] *Sinton-Instruments-BLS-BCT-400*, Sinton Instruments.

[10] R. Sinton, A. Cuevas, and M. Stuckings, "Quasi-steady-state photoconductance, a new method for solar cell material and device characterization," in *Proc. Conf. Record 25th IEEE Photovolt. Specialists*, 1996, pp. 457–460.

[11] A. B. Sproul, "Dimensionless solution of the equation describing the effect of surface recombination on carrier decay in semiconductors," *J. Appl. Phys.*, vol. 76, no. 5, pp. 2851–2854, 1994.

[12] A. D. Bristow, N. Rotenberg, and H. M. van Driel, "Two-photon absorption and kerr coefficients of silicon for 850-2200 nm," *Appl. Phys. Lett.*, vol. 90, no. 19, 2007, Art. no. 191104.

[13] D. Chung, B. Mitchell, M. Goodarzi, C. Sun, D. Macdonald, and T. Trupke, "Bulk lifetimes up to 20 ms measured on unpassivated silicon discs using photoluminescence imaging," *IEEE J. Photovolt.*, vol. 7, no. 2, pp. 444–449, Mar. 2017.

[14] F. D. Heinz, W. Warta, and M. C. Schubert, "Separation of the surface and bulk recombination in silicon by means of transient photoluminescence," *Appl. Phys. Lett.*, vol. 110, no. 4, 2017, Art. no. 042105.

[15] M. Rüdiger, T. Trupke, P. Würfel, T. Roth, and S. W. Glunz, "Influence of photon reabsorption on temperature dependent quasi-steady-state photoluminescence lifetime measurements on crystalline silicon," *Appl. Phys. Lett.*, vol. 92, no. 22, 2008, Art. no. 222112.

[16] T. Trupke *et al.*, "Temperature dependence of the radiative recombination coefficient of intrinsic crystalline silicon," *J. Appl. Phys.*, vol. 94, no. 8, pp. 4930–4937, 2003.

[17] D. Klaassen, "A unified mobility model for device simulation-I. model equations and concentration dependence," *Solid-State Electron.*, vol. 35, no. 7, pp. 953–959, 1992.

[18] D. Klaassen, "A unified mobility model for device simulation-II. temperature dependence of carrier mobility and lifetime," *Solid-State Electron.*, vol. 35, no. 7, pp. 961–967, 1992.

[19] F. D. Heinz, M. Kasemann, W. Warta, and M. C. Schubert, "Microscopic charge carrier lifetime in silicon from a transient approach," *Appl. Phys. Lett.*, vol. 107, no. 12, 2015, Art. no. 122101.

[20] H. Mackel and A. Cuevas, "Determination of the surface recombination velocity of unpassivated silicon from spectral photoconductance measurements," in *Proc. 3rd World Conf. Photovolt. Energy Convers.*, 2003, pp. 71–74.

[21] F. D. Heinz, T. Niewelt, and M. C. Schubert, "Experimental evidence of electron capture and emission from trap levels in Cz silicon," *Physica Status Solidi (A)*, vol. 214, no. 7, 2017, Art. no. 1700292.

[22] M. Tomassini *et al.*, "Recombination activity associated with thermal donor generation in monocrystalline silicon and effect on the conversion efficiency of heterojunction solar cells," *J. Appl. Phys.*, vol. 119, no. 8, 2016, Art. no. 084508.

[23] T. Trupke, R. A. Bardos, M. C. Schubert, and W. Warta, "Photoluminescence imaging of silicon wafers," *Appl. Phys. Lett.*, vol. 89, no. 4, 2006, Art. no. 044107.

[24] W. Shockley and W. T. Read, "Statistics of the recombinations of holes and electrons," *Phys. Rev.*, vol. 87, no. 5, pp. 835–842, 1952.